Multisource reverse time migration in anisotropic media

Wenyong Pan, Kris Innanen, Gary Margrave

ABSTRACT

Reverse Time Migration (RTM), a two-way wave equation method for accurate imaging, has attracted geophysicists' attention for many years for its great power in imaging the complex structures with dip angles. While seismic anisotropy in dipping shales can result in imaging and positioning problems for underlying structures. Isotropic RTM also suffers from seismic anisotropy. In this research, the pseudo-spectral method is used to solve the P-wave equation in Titled Transversely Isotropic (TTI) media for anisotropic RTM. Furthermore, RTM suffers from extensively computational cost for traditional shot by shot method, which limits its practical application considerably. The plane-wave source migration with densely distributed sources has been introduced in seismic imaging to reduce the computational cost. This strategy forms supergathers by summing densely distributed individual shots and can improve the efficiency of RTM considerably. While in practical application, the sources are always sparsely arranged. In this condition, the crosstalk artifacts which arise from the undesired interactions between unrelated shot and receiver wavefields will become very obvious. The phase encoding technique is introduced to shift or disperse these crossterms by slant stacking over sufficient number of ray parameters. In this research, we applied the phase encoded anisotropic RTM on Hess VTI (Vertical Transversely Isotropic) model. We also analyzed the influence of the number of encoded sources to the phase encoded images. And the imaging results for different phase encoding methods are also compared and discussed.

INTRODUCTION

Reverse-time migration (RTM) is a two-way wave equation migration method for accurate imaging in and below areas with both great structural and velocity complexities (Baysal et al., 1983; McMechan, 1983; Whitmore, 1983; Fletcher et al., 2009). It has virtually no dip limitation which makes it able to image the overturned reflections and handle all complex waveform multi-pathing. And it is increasingly used for refining structural boundaries during velocity model building.

For traditional seismic exploration, the subsurface layers are considered as isotopic medium which means that the velocity doesn't change with varying the directions. And the scalar acoustic wave equation can be solved efficiently to perform the acoustic RTM in isotropic media. While actually, the practical conditions are opposite for most interested areas, which is called seismic anisotropy. Seismic anisotropy is widely observed in seismic exploration activities and has been measured in shales, thin beds, and fractured rock formations (Jones and Wang, 1987; Thomsen, 1986; Johnston and Christensen, 1995; Leslie and Kaelin, 1999; Du, 2007). Conventional isotropic RTM for seismic imaging is insufficient in these areas (Fletcher et al., 2009). The most commonly considered type of anisotropy in seismic exploration is polar anisotropy which has an axis of symmetry perpendicular to the subsurface layers. So, this type of anisotropy is also called Vertical Transversely Isotropy (VTI)(Du, 2007). When the axis of symmetry is not vertical,the media is referred to as tilted transversely isotropic (TTI) media. Seismic anisotropy in dipping shales results in imaging and positioning problems for underlying structures. In this research, the pseudo-spectral method is used to solve the P-wave equation in Titled Transversely Isotropic (TTI) media for more accurate imaging results.

RTM also suffers from extensively computational burden for the traditional shot by shot method, which greatly limits its practical application. The plane-wave migration with dense sources was introduced in seismic imaging to reduce the computational cost (Morton and Ober, 1998; Romero et al., 2000; Zhang et al., 2005; Dai and Schuster, 2013). This strategy forms supergathers by summing densely distributed individual shots and can reduce the computational burden considerably. While in practical application, especially for 3D survey, the sources are sparsely sampled in the cross-line direction. In this condition, coherent crosstalk artifacts resulted from the undesired interactions between the unrelated source and receiver wavefields become very serious. The phase encoding strategy has been introduced to disperse these crosstalk artifacts with a sufficient number of ray parameters, which are controlled by the take-off angle at the surface location and the top surface velocity (Zhang et al., 2005; Tao and Sen, 2013; Dai and Schuster, 2013). Zhang et al. (2005) used the p component sampling theory to determine the number of rap parameters N_p under the assumptions that the shot sampling interval $\triangle p$ is small enough and the spread length $N_s \times \triangle p$ is great enough for marine data.

This paper is organized as follows: firstly, we reviewed basic theory for seismic anisotropy and the pseudo-spectral method used for anisotropic RTM. And then we reviewed the phase encoding strategies used to disperse the crosstalk artifacts. Finally, we applied the phase encoded anisotropic RTM on Hess VTI model. We compared the imaging results in isotropic media and anisotropic media using traditional shot-profile method. We discussed the influence of the number of encoded sources, and the number of slant parameters to phase encoded images. And the phase encoded imaging results with different phase encoding methods are also compared.

THEORY AND METHOD

Seismic anisotropy is the variation of velocity with direction, which is widely observed in seismic exploration activities. Polar anisotropy with a symmetric axis perpendicular to bedding is always involved in anisotropic imaging. The media is termed as Vertical Transversely Isotropy (VTI) when the axis of symmetry is vertical, as shown in Fig.1a. While when the symmetric axis is horizontal or titled, the media is termed as Horizontal Transversely Isotropy (HTI) and Titled Transversely Isotropy (TTI), as shown in Fig.1b and c respectively. Ignoring the tilted symmetry not only causes image blurring and mispositioning of the salt flank, but also distorts the base of salt and subsalt images (Huang et al., 2009).

Wave propagation in anisotropic media using pseudo-spectral method

Presently, the isotropic and VTI RTM has been widely studied in exploration geophysics. While the application of TTI RTM is impeded by some difficulties, one of which is the numerical formulations for non-vertical symmetric axes (Huang et al., 2009). The

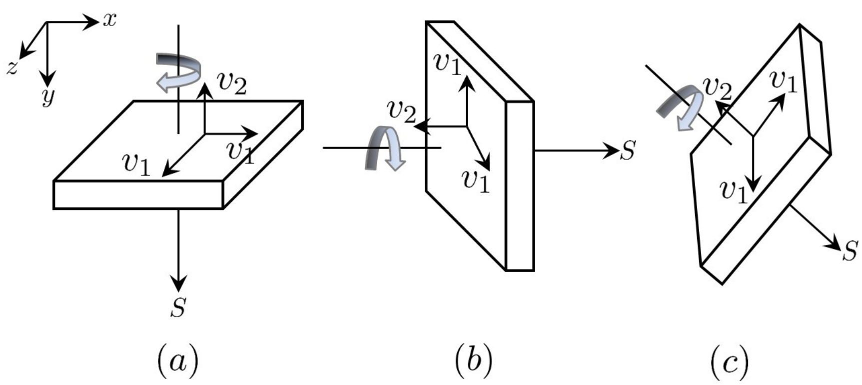

FIG. 1. (a), (b) and (c) show the VTI, HTI and TTI media respectively.

first thing is to derive the anisotropic wave equation (only P-wave is considered here) for implementing the TTI RTM method.

According to Hooke's Law:

$$\sigma_{ij} = c_{ijkl}\epsilon_{kl}, i, j = 1, 2, 3. \tag{1}$$

where σ is stress, ϵ is strain and c is the stiffness matrix. For most general anisotropic media there are 21 independent parameters in the stiffness matrix, as shown by equation (2). For isotropic media, there are 3 independent parameters, as shown by equation (3). While for VTI and TTI medias, there are 5 and 13 independent parameters in the stiffness matrix respectively, as shown by equation (4) and (5).

$$C = \begin{pmatrix} C_{11} & C_{12} & C_{13} & C_{14} & C_{15} & C_{16} \\ & C_{22} & C_{23} & C_{24} & C_{25} & C_{26} \\ & & C_{33} & C_{34} & C_{35} & C_{36} \\ & SYM & & C_{44} & C_{45} & C_{46} \\ & & & & C_{55} & C_{56} \\ & & & & & C_{66} \end{pmatrix} \tag{2}$$

$$C_{Isotropic} = \begin{pmatrix} C_{33} & C_{33}-2C_{44} & C_{33}-2C_{44} & 0 & 0 & 0 \\ C_{33}-2C_{44} & C_{33} & C_{33}-2C_{44} & 0 & 0 & 0 \\ C_{33}-2C_{44} & C_{33}-2C_{44} & C_{33} & 0 & 0 & 0 \\ 0 & 0 & 0 & C_{44} & 0 & 0 \\ 0 & 0 & 0 & 0 & C_{44} & 0 \\ 0 & 0 & 0 & 0 & 0 & C_{44} \end{pmatrix} \tag{3}$$

$$C_{VTI} = \begin{pmatrix} C_{11} & C_{12} & C_{13} & 0 & 0 & 0 \\ C_{12} & C_{11} & C_{13} & 0 & 0 & 0 \\ C_{13} & C_{13} & C_{33} & 0 & 0 & 0 \\ 0 & 0 & 0 & C_{44} & 0 & 0 \\ 0 & 0 & 0 & 0 & C_{44} & 0 \\ 0 & 0 & 0 & 0 & 0 & C_{44} \end{pmatrix} \tag{4}$$

$$C_{TTI} = \begin{pmatrix} C'_{11} & C'_{12} & C'_{13} & 0 & C'_{15} & 0 \\ C'_{12} & C'_{22} & C'_{23} & 0 & C'_{25} & 0 \\ C'_{13} & C'_{23} & C'_{33} & 0 & C'_{35} & 0 \\ 0 & 0 & 0 & C'_{44} & 0 & C'_{46} \\ C'_{15} & C'_{25} & C'_{35} & 0 & C'_{55} & 0 \\ 0 & 0 & 0 & C'_{46} & 0 & C'_{66} \end{pmatrix} \tag{5}$$

Tsvankin (1996) gave the exact phase-velocity function expressed through the Thomsen parameters:

$$\frac{v^2(\theta)}{v_{p0}^2} = 1 + \varepsilon \sin^2\theta - \frac{f}{2} + \frac{f}{2}\sqrt{1 + \frac{4\sin^2\theta}{f}\left(2\delta\cos^2\theta - \varepsilon\cos 2\theta\right) + \frac{4\varepsilon^2\sin^4\theta}{f^2}} \tag{6}$$

where $v(\theta)$ is the phase velocity, θ is the phase angle measured from the symmetry axis, v_{p0} is the vertical velocity, ε and δ are the Thomsen parameters and $f = 1 - \frac{v_{s0}^2}{v_{p0}^2}$. Equation (2) can be simplified further by separating out under the radical a "non-elliptical" term containing $\varepsilon - \delta$ (Tsvankin, 1996):

$$\frac{v^2(\theta)}{v_{p0}^2} = 1 + \varepsilon \sin^2\theta - \frac{f}{2} + \frac{f}{2}\sqrt{(1 + \frac{2\varepsilon\sin^2\theta}{f})^2 - \frac{2(\varepsilon - \delta)\sin^2(2\theta)}{f}}, \tag{7}$$

If we rotate the vertical axis of symmetry by an angle of ϕ, we can get the phase velocity equation for TTI media which can be written as:

$$\frac{v^2(\theta,\phi)}{v_{p0}^2} = 1 + \varepsilon \sin^2(\theta-\phi) - \frac{f}{2} + \frac{f}{2}\sqrt{(1 + \frac{2\varepsilon\sin^2(\theta-\phi)}{f})^2 - \frac{2(\varepsilon - \delta)\sin^2\left(2(\theta-\phi)\right)}{f}}, \tag{8}$$

To simplify the phase velocity equation further, we can expanded the radical in a Taylor series and dropped the quadratic and higher terms of the anisotropy parameters ε and δ. Then the simplified phase velocity equation can be written as (Du, 2007):

$$\frac{v^2(\theta,\phi)}{v_{p0}^2} = 1 + 2\delta\sin^2(\theta-\phi)\cos^2(\theta-\phi) + 2\varepsilon\sin^4(\theta-\epsilon), \tag{9}$$

If we multiply equation (5) with the wavefield in Fourier domain $U\left(k_x, k_z, t\right)$ and apply an inverse Fourier transform in frequency, then we obtain the P-wave equation in time-wavenumber domain for TTI media (Du, 2007):

$$\frac{\partial^2 U_p(k_x,k_z,t)}{\partial t^2} = -v_{p0}^2\left(k_x^2 + k_z^2 + A + B + C + D + E\right)U_p(k_x,k_z,t), \tag{10}$$

where

$$
\begin{aligned}
A &= \left(2\delta \sin^2\phi \cos^2\phi + 2\varepsilon \cos^4\phi\right) \frac{k_x^4}{k_x^2 + k_z^2}, \\
B &= \left(2\delta \sin^2\phi \cos^2\phi + 2\varepsilon \sin^4\phi\right) \frac{k_x^4}{k_x^2 + k_z^2}, \\
C &= \left(-\delta \sin^2(2\phi) + 3\varepsilon \sin^2 2\phi + 2\delta \cos^2\phi\right) \frac{k_x^2 k_z^2}{k_x^2 + k_z^2}, \\
D &= \left(\delta \sin^4\phi - 4\varepsilon \sin(2\phi) \cos^2\phi\right) \frac{k_x^3 k_z}{k_x^2 + k_z^2}, \\
E &= -\left(\delta \sin^4\phi - 4\varepsilon \sin(2\phi) \sin^2\phi\right) \frac{k_z^3 k_x}{k_x^2 + k_z^2}.
\end{aligned}
\tag{11}
$$

Here, the pseudo-spectral method (Fletcher et al., 1987) is introduced to solve the P-wave equation in TTI media. Pseudo-spectral method has equivalent accuracy comparing with high order of finite difference method but it needs less number of grid points in each spatial direction and less memory and running time. To implement this method numerically, firstly, we can apply a two dimensional Fourier transform for transforming the data from spatial domain to wave-number domain and accomplish the wave-number computation. Then, apply an inverse Fourier transform and return to spatial domain for anisotropic parameters calculation. Finally, we can calculate the wavefield in time domain. The flow chart of pseudo-spectral method is show in Figure 2.

$$
\begin{tikzcd}
U(x,z,t) \arrow[d, "FFT"] & U(x,z,t-\Delta t) \\
U(k_x,k_z,t) \arrow[d] & U''(x,z,t) \arrow[u, "FD"'] \\
U'(k_x,k_z,t) \arrow[r, "IFFT"] & U'(x,z,t) \arrow[u, "TTI\ \text{Parameters}"']
\end{tikzcd}
$$

FIG. 2. Flow chart for pseudo-spectral method.

Fig.3 illustrate a numerical example for wave propagation in anisotropic media using the pseudo-spectral method. The velocity model is $8km$ in width and $4km$ in depth with a constant background velocity of $2.5km/s$. And the Thomsen parameters are $\varepsilon = 0.15$ and $\delta = 0.18$. The source is located at $(4km, 0km)$. Fig.3a shows the snapshot in VTI media when the titled angle $\phi = 0^o$ and Fig.3b, c and d show the snapshots when the titled angle is 30^o, 60^o, and 90^o respectively.

Plane-Wave Migration

The traditional shot-profile reverse time migration can provide high quality images but typically at a greater cost (Romero et al., 2000). The plane-wave source migration with slant stacking (or delayed shot migration) has been introduced to reduce the computational

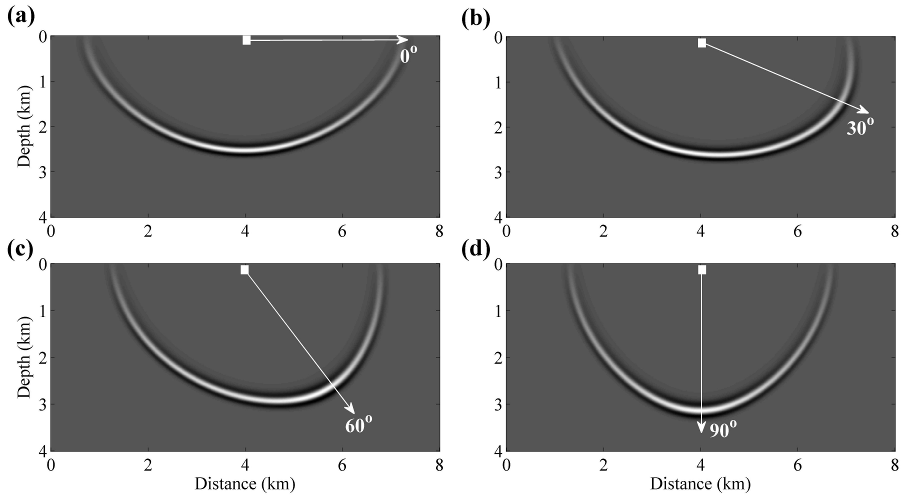

FIG. 3. Snapshots in anisotropic media. (a) Snapshot in VTI media ($\phi = 0^o$); (b) Snapshot in TTI media ($\phi = 30^o$); (c) Snapshot in TTI media ($\phi = 60^o$); (d) Snapshot in TTI media ($\phi = 90^o$).

burden (Morton and Ober, 1998; Romero et al., 2000; Zhang et al., 2005; Dai and Schuster, 2013) and it is implemented by applying phase shifts at densely distributed sources. The linear phase shifts are controlled by the ray parameters and sources locations. In theory, the plan-wave migration image is identical to the traditional shot-profile migration image with sufficient ray parameters p and small enough source interval $\triangle x_s$ (Liu et al., 2002, 2006; Shan et al., 2009).

However, in practical application, the sources are always sparsely distributed and the shot gathers are far away from each other, especially in the crossline direction of a 3D survey. When the sources are distributed densely and regularly in the whole acquisition geometry, the plane-wave migration shows a limited amount of noise (Liu et al., 2006). While when the shots are sparsely and irregularly sampled, the crosstalk noise arising form the undesired interactions between the unrelated sources and receivers wavefields becomes a problem. Plane-wave migration with sparsely sampled sources can be named as pseudo plane-wave migration or phase encoded source migration. The phase encoding strategy is introduced to disperse or shift these crosstalk noise for sparsely sampled experiments. We analyzed the influence of the source interval $\triangle x_s$ to the phase encoded image.

With decreasing the number of encoded sources N_s or increasing the source sampling interval $\triangle x_s$, the crosstalk terms become weaker. While if the sources distribution is highly sparse, the final image can not cover the whole subsurface. So, in practical application, a set number of sources will be arranged. And the phase encoded source migration image with sufficient slant parameter stacking is also equivalent to a shot-profile migration image (Shan, 2008; Shan et al., 2009). Generally, the pseudo plane-wave sources with small take-off angles mainly illuminate or image the reflectors that are almost horizontal. And the pseudo plane-wave sources with large take-off angles are responsible to image or illuminate the steep reflectors.

Plane-wave extrapolation in titled coordinate system

Shan (2008) introduced the plane-wave extrapolation in titled coordinate system for plane-wave migration. Fig.4a shows the VTI media in the traditional Cartesian coordinate system as indicated by (X, Z) and Fig.4b shows the VTI media in the titled coordinate system with a take-off angle of θ, as indicated by (X', Z'). For plane-wave migration in titled coordinate system, each plane-wave source (or ray parameter) has its own coordinate system such that the extrapolation direction is closer to the propagation directions, and the steep structures can be well imaged.

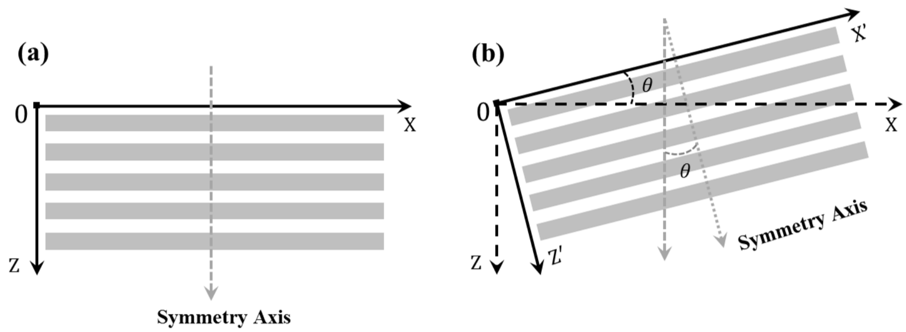

FIG. 4. VTI media in Cartesian coordinate system (a) and VTI media in titled coordinates system (b). (X, Z) and (X', Z') indicate the Cartesian coordinate system and titled coordinate system respectively.

Fig.5a and b show the wavefield snapshots in anisotropic media when the sources are sparsely arranged and densely arranged respectively with ray parameter $p = 0.2s/km$. The Thomsen parameters are $\delta = 0.18$, $\varepsilon = 0.15$ and $\phi = 45^o$.

Pseudo plane-wave source migration or phase encoded source migration

When the sources are sparsely distributed, the phase encoding method can be employed to disperse or shift the crosstalk artifacts caused by the undesired interactions between unrelated source and receiver wavefield. The linear phase encoding technique is performed by applying linear phase shifts (or time delays in time domain) to the shot records. The phase shift function $\gamma(x_s, p, w) = \omega p(x_s - x_0)$ is controlled by the ray parameter (or slant parameter) p and source's position x_s, as shown in Fig.6. Generally, sufficient ray parameters can disperse or reduce these crosstalk terms effectively. And a common-receiver gather is transformed into a single trace from a linear source wavefields by $\tau - p$ transform (Zhang et al., 2005):

$$\tilde{\mathbf{d}}\left(\mathbf{r}_g, \mathbf{r}_s, p, \omega\right) = \int \mathbf{d}\left(\mathbf{r}_g, \mathbf{r}_s, \omega\right) e^{i\omega p(x_s - x_0)} d\mathbf{r}_s \tag{12}$$

where $\mathbf{r}_g = (x_g, y_g = 0, z_g = 0)$ and $\mathbf{r}_s = (x_s, y_s = 0, z_s = 0)$ mean the locations of the receivers and sources. Actually, equation (12) can be considered as a Fourier transform, replacing the wavenumber k with ωp. This theory can be used to determine the ray parameter spacing $\triangle p$ for slant stacking (Zhang et al., 2005).

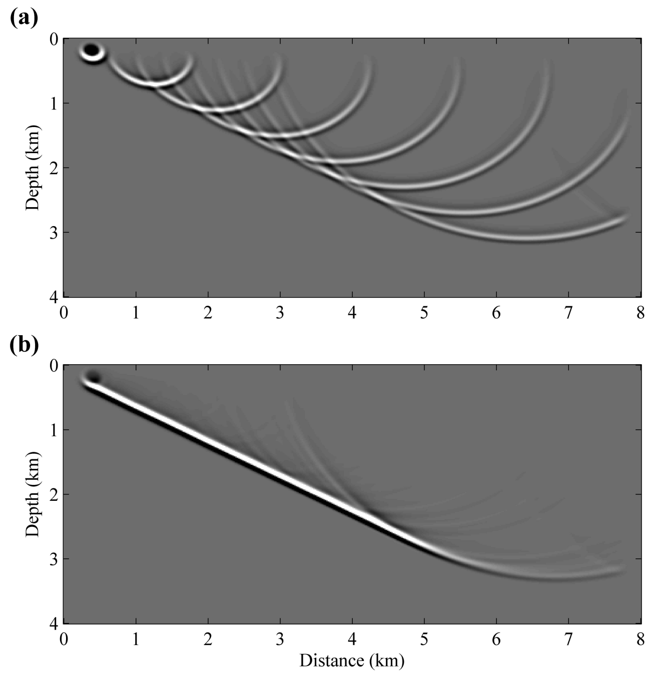

FIG. 5. The snapshots in anisotropic media for sparse sources arrangement (a) and dense sources arrangement (b) with ray parameter $p = 0.2s/km$. The Thomsen parameters $\delta = 0.18$, $\varepsilon = 0.15$ and $\phi = 45^o$. This figure is produced following Shan et al. (2009).

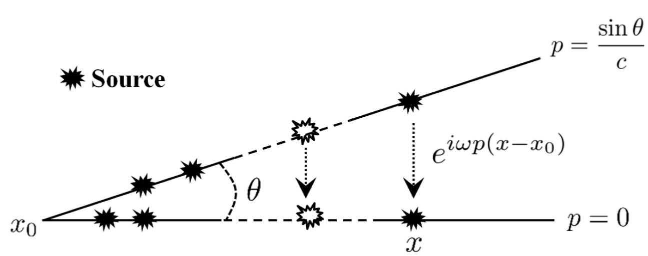

FIG. 6. Diagram for linear phase encoding strategy reproduced from (Zhang et al., 2005; Dai and Schuster, 2013).

The forward modeling wavefields and backpropagated wavefields with linear phase encoding can be written as (Zhang et al., 2005; Tao and Sen, 2013):

$$\mathbf{D}\left(\mathbf{r}, \mathbf{r}_s, p_i, \omega\right) = \sum_{\mathbf{r}_s} \tilde{G}\left(\mathbf{r}, \mathbf{r}_s, \omega\right) A(\omega) e^{i\omega p_i (\mathbf{r}_s - \hat{\mathbf{r}})}, \tag{13}$$

$$\mathbf{U}\left(\mathbf{r}, \mathbf{r}'_s, p_i, \omega\right) = \sum_{\mathbf{r}'_s} \bar{G}\left(\mathbf{r}, \mathbf{r}'_s, \omega\right) A(\omega) e^{i\omega p_i (\mathbf{r}'_s - \hat{\mathbf{r}})}, \tag{14}$$

where i is the index of the slant parameter. $\mathbf{r}_s$ and $\mathbf{r}'_s$ are the sources' locations. $A(\omega)$ is the real function depending upon the angular frequency ω (Liu et al., 2006; Tang, 2009). And when $p_i \geq 0$, $\hat{\mathbf{r}} = \mathbf{r}_0$. When $p_i < 0$, $\hat{\mathbf{r}} = \mathbf{r}_{max}$. Then applying a zero-lag corsscorrelation imaging condition between the forward modeling wavefields $\tilde{\mathbf{G}}\left(\mathbf{r}, \mathbf{r}_s, p_i, \omega\right)$ and backpropagated wavefields $\bar{\mathbf{G}}\left(\mathbf{r}, \mathbf{r}'_s, p_i, \omega\right)$ gives the image for ray parameter p_i:

$$I\left(\mathbf{r}, p_i\right) = \sum_{\omega} \sum_{\mathbf{r}_s} \sum_{\mathbf{r}'_s} \Re \left\{ \omega^2 \mid A(\omega) \mid^2 \mathbf{D}\left(\mathbf{r}, \mathbf{r}_s, p_i, \omega\right) \mathbf{U}^*\left(\mathbf{r}, \mathbf{r}'_s, p_i, \omega\right) \right\}, \tag{15}$$

Then substituting equation (13) and (14) into equation (15):

$$I\left(\mathbf{r}, p_i\right) = \sum_{\omega} \sum_{\mathbf{r}_s} \sum_{\mathbf{r}'_s} \Re \left\{ \omega^2 \mid A(\omega) \mid^2 \tilde{G}\left(\mathbf{r}, \mathbf{r}_s, \omega\right) \bar{G}^*\left(\mathbf{r}, \mathbf{r}'_s, \omega\right) e^{i\omega p_i (\mathbf{r}_s - \mathbf{r}'_s)} \right\}, \tag{16}$$

In equation (15), when $\mathbf{r}_s = \mathbf{r}'_s$, the linear phase encoded image $I\left(\mathbf{r}, p_i\right)$ is equal to the conventional common shot image $I_{cs}\left(\mathbf{r}\right)$. And when $\mathbf{r}_s \neq \mathbf{r}'_s$, the linear phase encoded image $I\left(\mathbf{r}, p_i\right)$ becomes the cross terms I_{cross}. So, the linear phase encoded image can be written as a summation of the conventional common shot image and the the cross talk artifacts:

$$I\left(\mathbf{r}, p_i\right) = I_{cs}\left(\mathbf{r}\right) + I_{cross}, \tag{17}$$

To disperse the second term in the above equation, we can construct the image by slant stacking all of the possible ray parameters:

$$\tilde{I}\left(\mathbf{r}\right) = \sum_{\omega} \sum_{\mathbf{r}_s} \sum_{\mathbf{r}'_s} \sum_{p=-\infty}^{+\infty} \Re \left\{ \omega^2 \mid A(\omega) \mid^2 \tilde{G}\left(\mathbf{r}, \mathbf{r}_s, \omega\right) \bar{G}^*\left(\mathbf{r}, \mathbf{r}'_s, \omega\right) e^{i\omega p (\mathbf{r}_s - \mathbf{r}'_s)} \right\}, \tag{18}$$

And because summing the linear phase shifts over all ray parameters in three dimensions gives (Liu et al., 2006; Tang, 2009; Tao and Sen, 2013):

$$\sum_{p=-\infty}^{+\infty} e^{i\omega p (\mathbf{r}_s - \mathbf{r}'_s)} = \frac{1}{\mid \omega \mid^2} \delta\left(\mathbf{r}_s - \mathbf{r}'_s\right), \tag{19}$$

Hence, equation (17) becomes:

$$\tilde{I}\left(\mathbf{r}\right) = \sum_{\omega} \sum_{\mathbf{r}_s} \Re \left\{ \omega^2 \tilde{G}\left(\mathbf{r}, \mathbf{r}_s, \omega\right) \bar{G}^*\left(\mathbf{r}, \mathbf{r}'_s, \omega\right) \right\} = I\left(\mathbf{r}\right), \tag{20}$$

While summing the linear phase encoded image over all ray parameters is computationally expensive. So, setting appropriate ray parameter range and spacing for phase encoding is necessary. Generally, the ray parameter range can be determined by the steep angles of the geological structures. Different take-off angles are responsible to illuminate or image the geological structures with different steep angles. And the sample interval $\triangle p$ can be determined by the p component sampling theory (Zhang et al., 2005). And the positive and negative ray parameters, as indicated by Fig.7, can be used to image the structures with different deep directions.

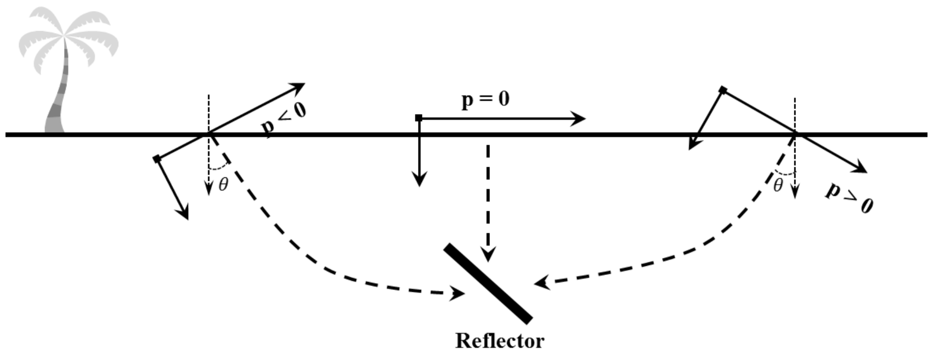

FIG. 7. Plane-wave sources with ray parameter $p < 0$, $p = 0$ and $p > 0$ respectively.

Slant parameter component sampling theory

As we mentioned above, the ray parameter range can be determined by the deep angles of the subsurface structures. In practical application, a set of ray parameters should be defined by to make the phase encoded migration image equivalent to the traditional shot-profile image. And the number ray parameters N_p and ray parameter interval $\triangle p$ can be defined by the p component sampling theory by (Zhang et al., 2005):

$$N_p \geq \frac{N_s \triangle x_s f\left(\sin\alpha_2 - \sin\alpha_1\right)}{v}, \tag{21}$$

$$\triangle p = \frac{\left(\sin\alpha_2 - \sin\alpha_1\right)}{v N_p}, \tag{22}$$

where N_s and $\triangle x_s$ are the number of encoded sources and source interval. And $N_s \times \triangle x_s$ is the spread length. $f = \frac{\omega}{2\pi}$ is the frequency. v is the top surface velocity. α_1 and α_2 are the take-off angles.

Random phase encoding method

Comparing with the linear phase variation for the linear phase encoding strategy, random phase encoding method is implemented by applying random phase shifts on different sources to disperse or shift the crosstalk terms. The phase functions $\gamma(\mathbf{r}, \mathbf{n}, \omega)$ in the random phase encoding method are random numbers from 0 to 2π, where **n** means the number of realizations. So, when stacking over **n**, the crosstalk noise can be attenuated effectively:

$$\sum_{\mathbf{n}=-\infty}^{+\infty} e^{i\gamma(\mathbf{r},\mathbf{n},\omega)} = 1, \tag{23}$$

Hybrid or chirp phase encoding method

Chirp source encoding method is a combination of linear source encoding method and random source encoding method (Pan et al., 2014) and it is implemented by adding a random term to the phase functions in linear phase encoding method. And the phase shift can be written as:

$$e^{i\omega(p+\epsilon\triangle p)(\mathbf{r}'-\mathbf{r})}, \tag{24}$$

where ϵ is small random scalar to control the ray parameter perturbation $\triangle p$.

NUMERICAL EXPERIMENTS

Fig.8 shows the TTI Thrust model for numerical experiments used in this research. The model has 200×300 grid cells with $6km$ in horizontal and $2km$ in depth. The horizontal spacing is $20m$ and the vertical spacing is $10m$. The TI trust sheet was divided into 4 blocks with different titled angles (0^o, 30^o, 51^o, and 61^o) (Fletcher, 2009), and the anisotropic parameters are $\varepsilon = 0.15$ and $\delta = 0.08$. The four blocks with a velocity of $2925m/s$ are embedded in isotropic background with a constant velocity of $2740m/s$. We compare the imaging results with one source located at $(3km, 0km)$ in TTI media, VTI media and isotropic media respectively, as shown by Fig.9a, b and c. Here, we just extract the imaging results from $1km$ to $2.2km$ in vertical and $2km$ to $4km$ in horizontal. It can be seen that the imaging results in VTI media (Fig.9b) and isotropic media (Fig.9c) cannot image the structures correctly and the positions of the structures are distorted, as indicated by the blue boxes.

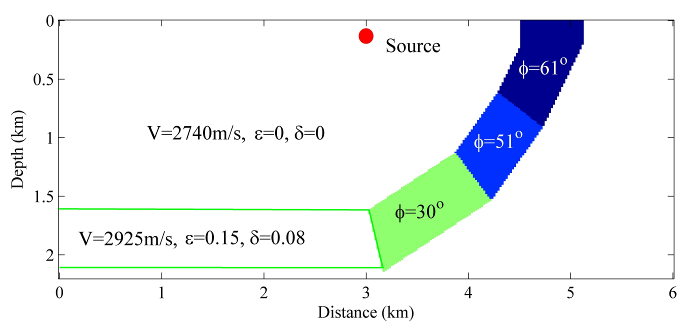

FIG. 8. TTI Thrust model.

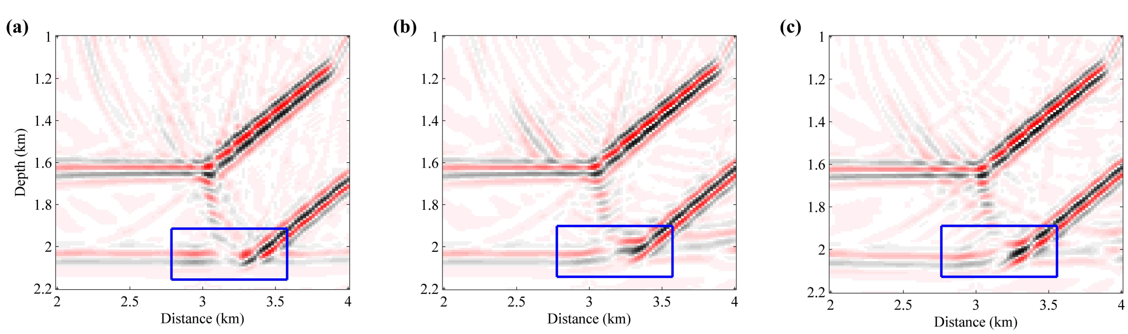

FIG. 9. RTM imaging results in anisotropic media and isotropic media. (a) shows the imaging result in TTI media; (b) is the imaging result in VTI media; (c) is the imaging result in isotropic media.

Fig.10 shows the Hess VTI model used in this research. Fig.10a, b and c indicate the P-wave velocity model, Thomsen parameters δ and ε respectively. The resampled Hess VTI model has 300×724 grid cells with the same grid interval of $20m$ in horizontal and vertical. We tested the sensitivity to the number of encoded sources using linear source encoding method when the ray parameter $p = 0$. 724 receivers are distributed from $0km$ to $14.48km$ regularly with a spacing of $20m$ in the whole geometry. Fig.10a, b and c show the P-wave velocity model, Thomsen parameter δ and ε respectively.

In Fig.11, we compared the wavefields when wave propagating in isotropic and anisotropic media using one single source located at $7km$ in horizontal. Fig.11a, c and e show the snapshots at $0.25s$, $0.5s$ and $0.75s$ when the wave propagating in the isotropic media. Fig.11b, d and f show the snapshots at $0.25s$, $0.5s$ and $0.75s$ when the wave propagating in the anisotropic media. Fig.12a and b show the seismic shot gather in the isotropic and anisotropic media respectively. It is easy for us to recognize the differences when wave propagating in different type medias. VTI model can describe the subsurface formations better. The inaccuracy of the isotropic model can result in mispositionings when imaging the subsurface structures.

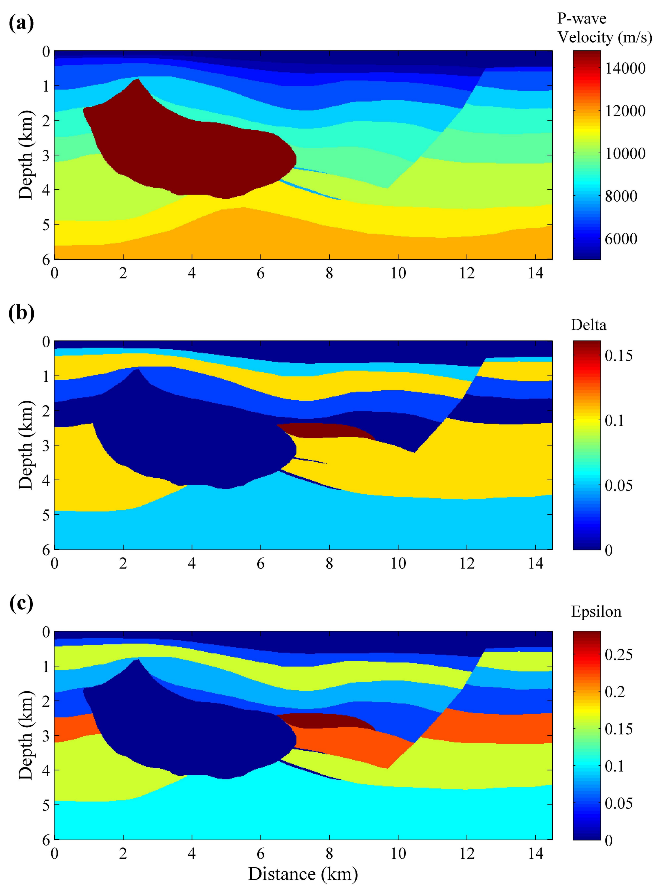

FIG. 10. Hess VTI model. (a) is the P-wave velocity model. (b) and (c) are the Thomsen parameters δ and ε respectively.

Firstly, we compared the imaging results in isotropic media and anisotropic media respectively when using traditional shot by shot method. Fig.13a shows the imaging result

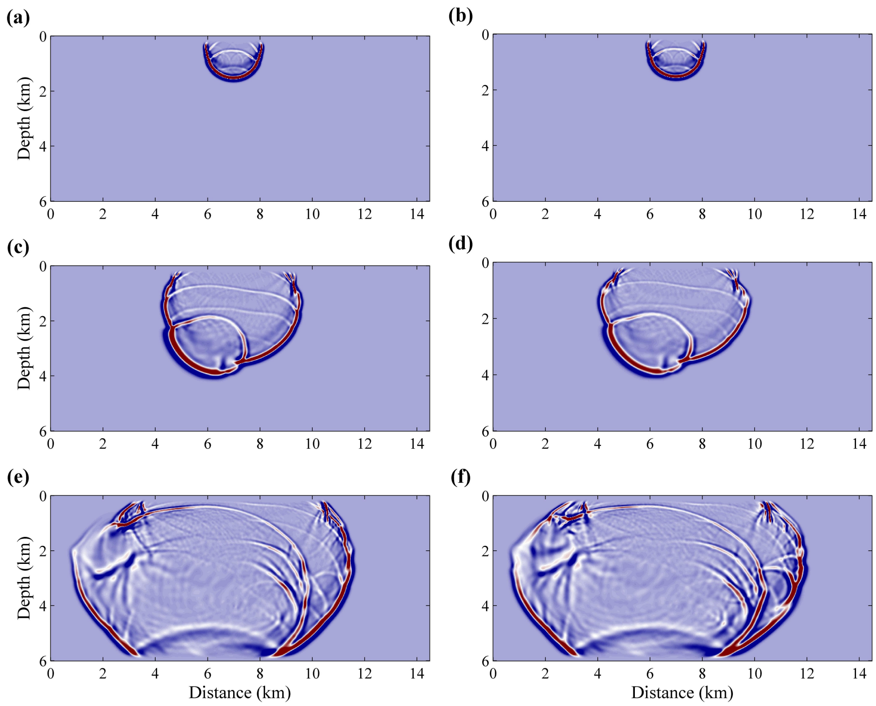

FIG. 11. Comparison of snapshots in isotropic and anisotropic media. (a), (c) and (e) are the snapshots in isotropic media when the time step is $0.25s$, $0.5s$ and $0.75s$ respectively. (b), (d) and (f) are the snapshots in anisotropic media when the time step is $0.25s$, $0.5s$ and $0.75s$ respectively.

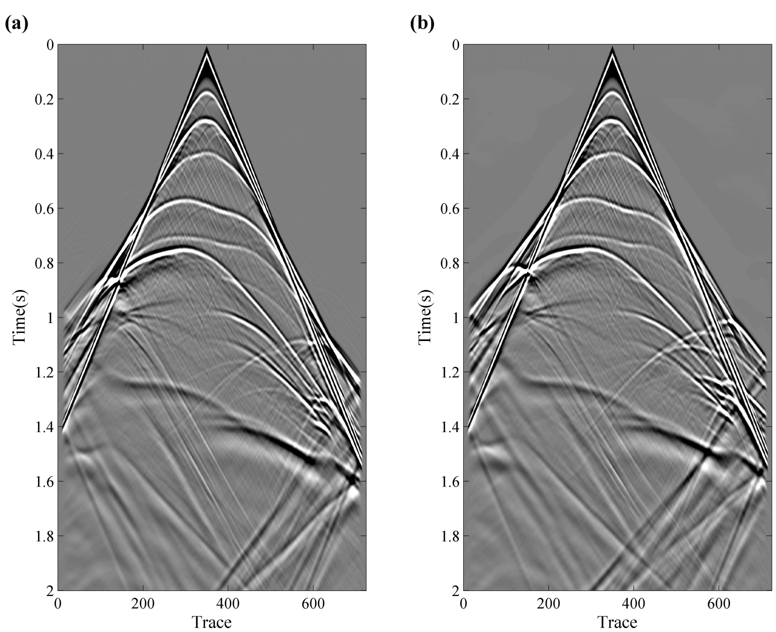

FIG. 12. Comparison of shot records in isotropic (a) and anisotropic (b) media respectively.

formed by crosscorrelating the forward modeling wavefields and backpropagated wavefields just using the P-wave velocity model. We can see that the geological structures and faults are imaged very well compared to the true P-wave velocity model. While it may miss some structures where have anomalies in Thomsen parameters δ or ε, as indicated by the blue arrow in Fig.13c. Fig. 13b and c show the imaging results in the isotropic media and VTI media respectively. We can see that the image in isotropic media suffers from mispositioning problem, as indicated by the green arrows. While the subsurface structures in Fig.10c can be imaged very well.

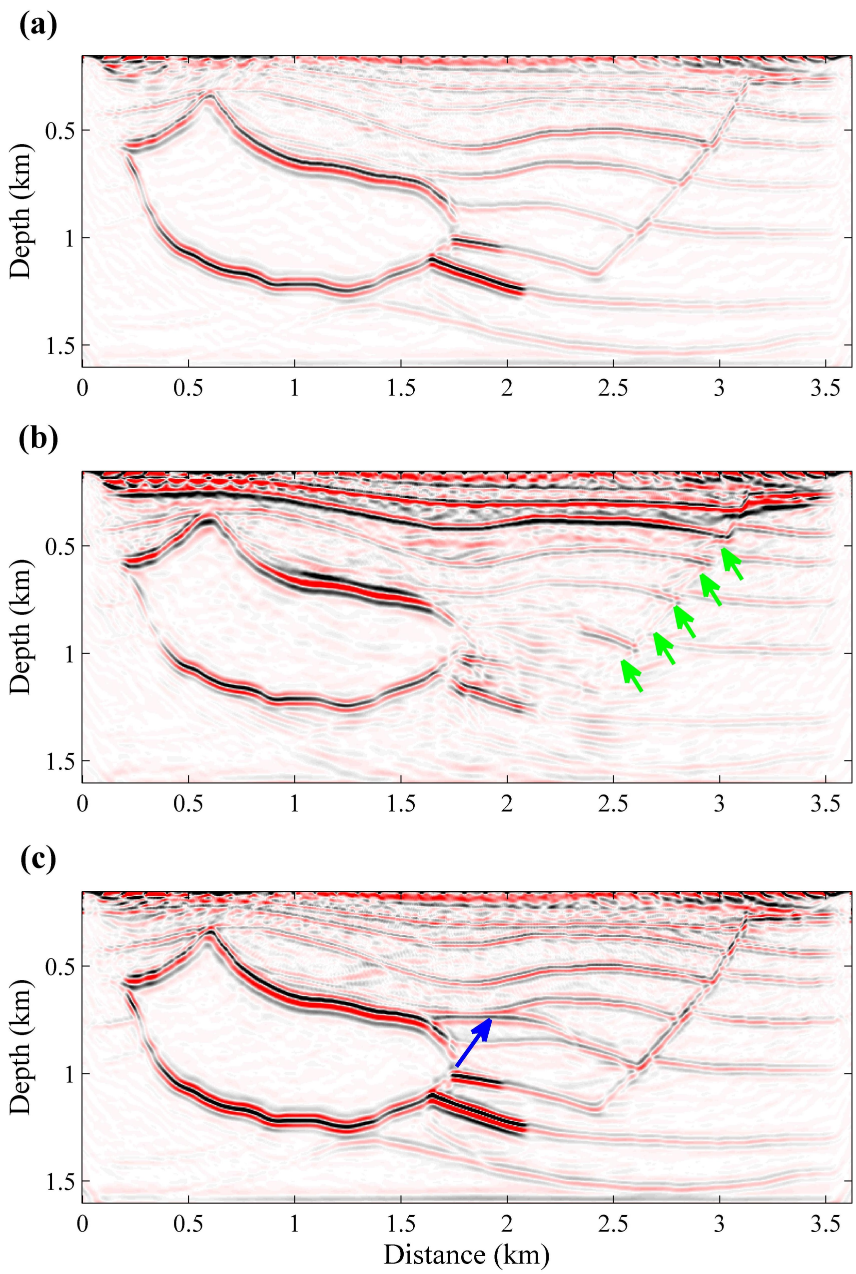

FIG. 13. Imaging results comparison. (a) is the imaging result when just using the P-wave velocity shown in Fig.10a; (b) is the imaging result using isotropic model; (c) is the imaging result using VTI model.

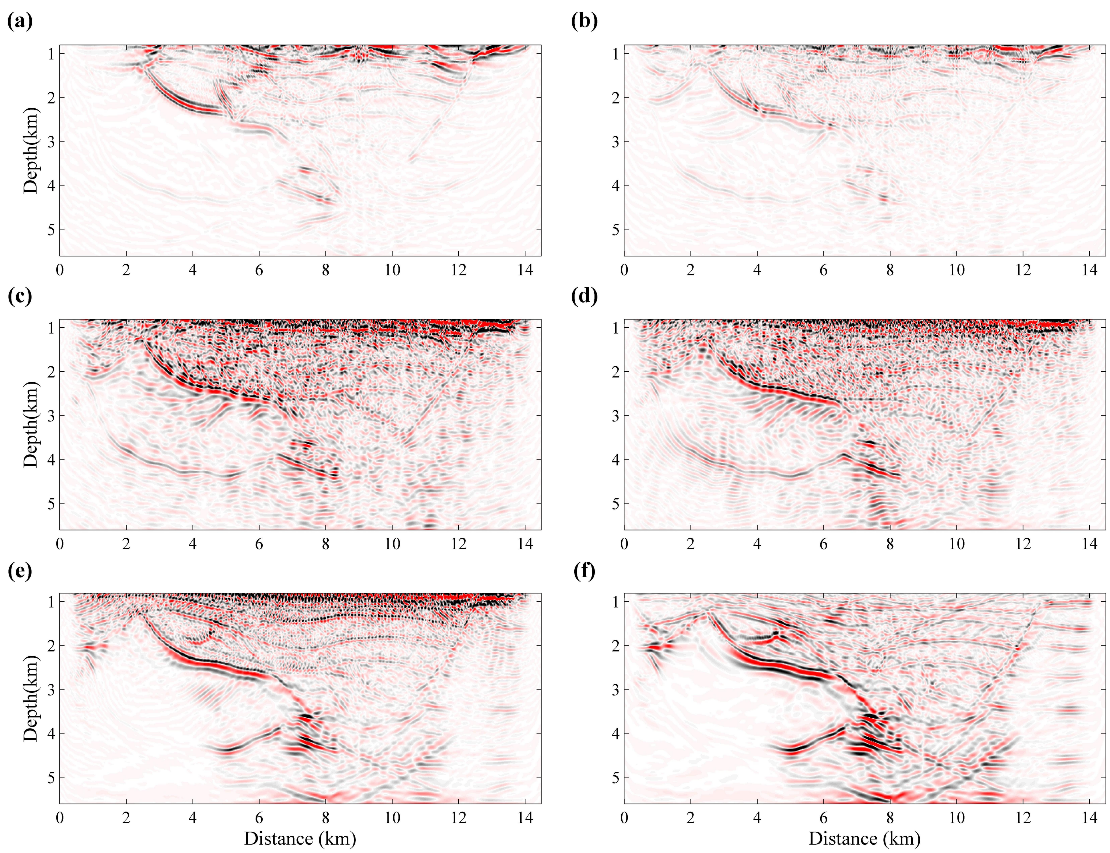

FIG. 14. Imaging results comparison for different number of sources. The encoded source number in (a), (b), (c), (d), (e) and (f) are 3, 7, 14, 36, 72 and 350 respectively.

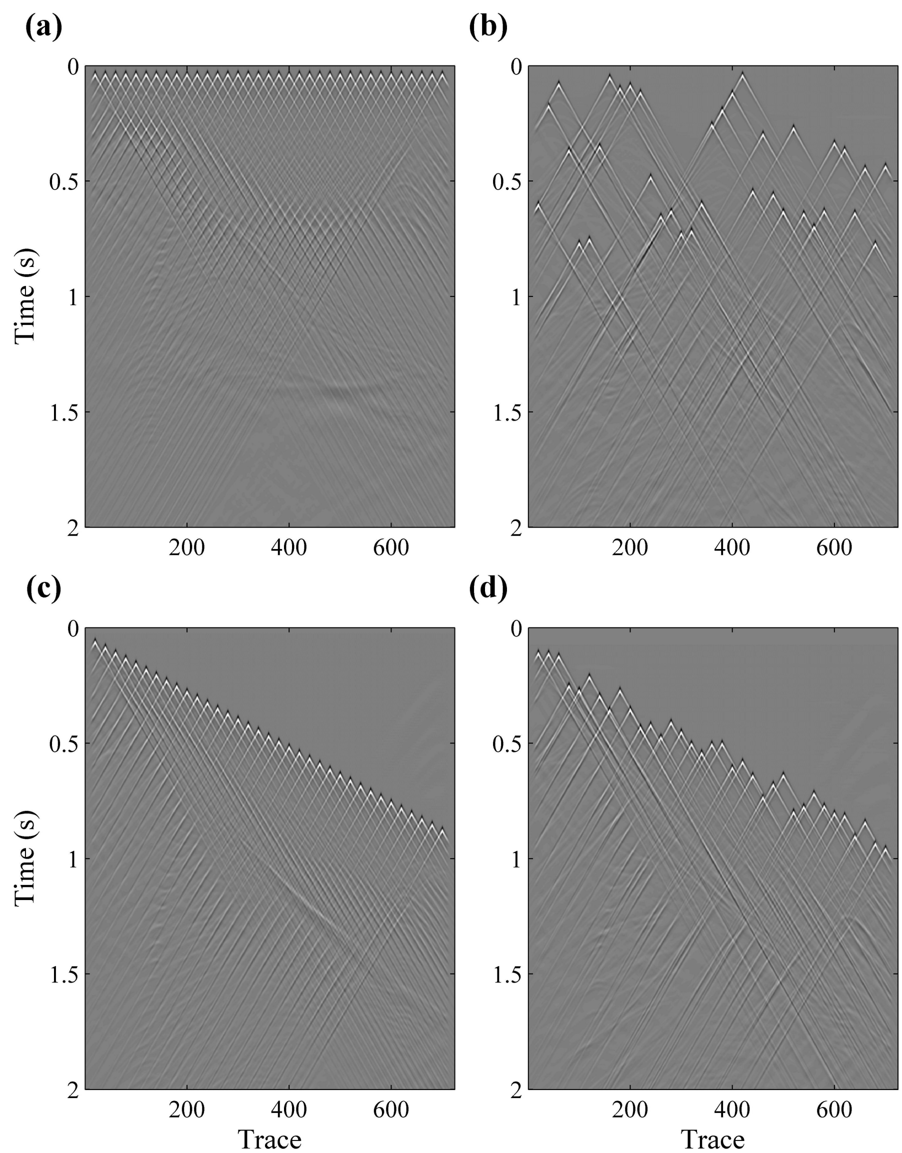

FIG. 15. Supergathers comparison. (a) is the supergather obtained by linear phase encoding method when ray-parameter $p = 0$; (b) is the supergather formed by random phase encoding method; (c) and (d) are the supergathers for linear phase encoding method and dithered phase encoding method when ray parameter $p = 0.06s/km$. And the source number N_s is 37.

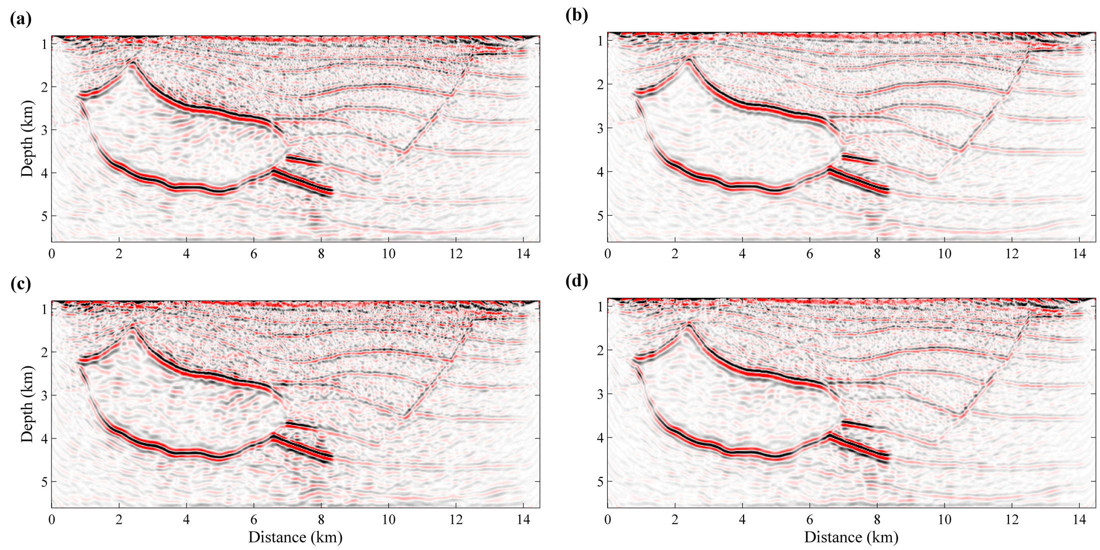

FIG. 16. (a) and (c) are the imaging results by linear and chirp phase encoding methods with 7 simulations ranging the ray parameter from $-0.06s/km$ to $0.06s/km$ with a step of $0.02s/km$. (b) and (d) are the imaging results by linear and chirp phase encoding methods with 13 simulations ranging the ray parameter from $-0.06s/km$ to $0.06s/km$ with a step of $0.01s/km$. 37 sources are arranged from $0.4km$ to $14km$ with a spacing of $0.4km$.

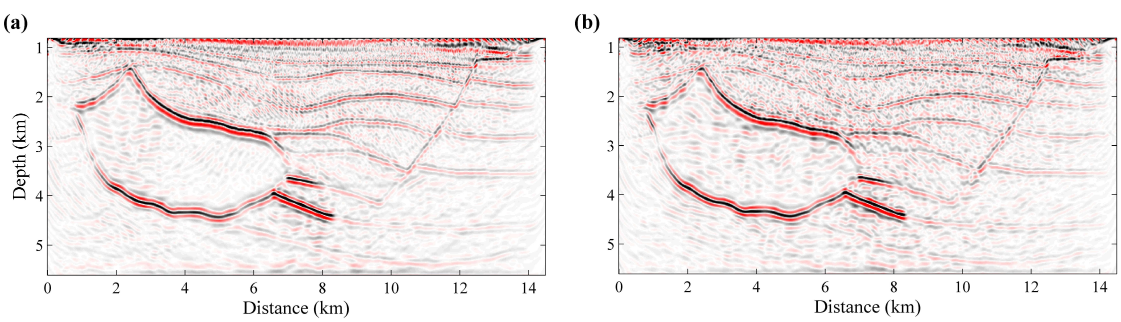

FIG. 17. (a) and (b) are the imaging results by linear phase encoding method and chirp phase encoding method with 7 simulations ranging the ray parameter from $-0.06s/km$ to $0.06s/km$ with a step of $0.02s/km$. 71 sources are arranged from $0.2km$ to $14km$ with a spacing of $0.2km$.

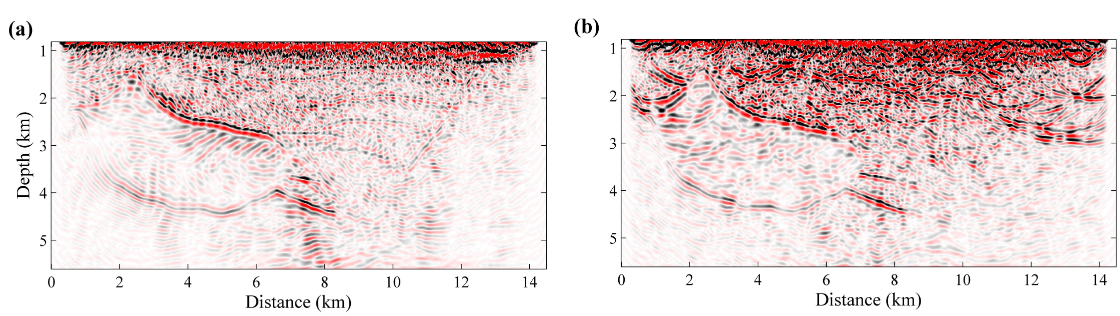

FIG. 18. (a) and (b) are the imaging results using linear phase encoding method with ray parameter $p = 0$ and random phase encoding method. And the source number N_s is 37.

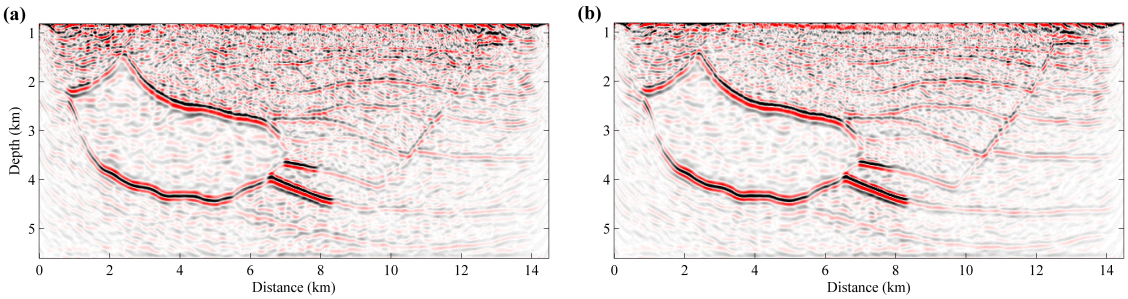

FIG. 19. (a) and (b) are the imaging results by random phase encoding method with 7 and 13 simulations respectively. And the source number N_s is 37.

Fig.14a, b, c, d, e and f show the imaging results when the number of encoded sources is 3, 7, 14, 36, 72 and 350 respectively with ray parameter $p = 0$. We can recognize that when the sources are highly sparsely distributed (e.g.$N_s = 3$ and 7), the crosstalk noise in the shallow parts of the image can hard be observed. Furthermore, we can note that the amplitudes for the deep parts of the reflectors are very week. While with increasing the number of encoded sources N_s (e.g.$N_s = 14$, 36 and 72), the crosstalk noise in the shallow parts of the image become very obvious and the amplitudes for the deep reflectors become stronger. While the resolution of image has been decreased with increasing the number of encoded sources. Fig.14f shows the image with highly dense sources' distribution $(N_s = 350)$. The plane-wave image shows a limited amount crosstalk noise, while some structures with deep angles cannot be imaged and some aliasing artifacts exist. Fig.15 show the supergathers

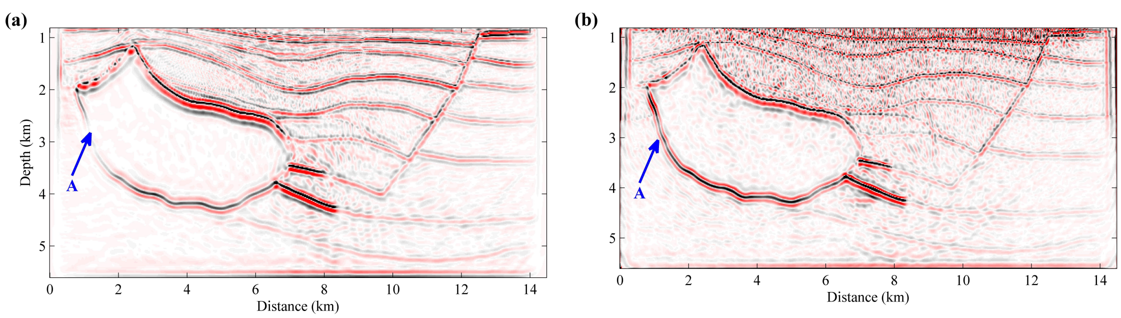

FIG. 20. (a) and (b) are the imaging results by linear and chirp phase encoding methods respectively with 7 simulations when the number of encoded sources N_s is 350.

with the encoded sources number $N_s = 37$ by different phase encoding methods. Fig.15a and c are the supergathers for linear phase encoding method with ray parameter $p = 0$ and $p = 0.06s/km$ respectively. And Fig.15c and d show the supergathers by random phase encoding method and chirp phase encoding method respectively.

Fig.16a and c are the imaging results by linear phase encoding method and chirp phase encoding method with 7 realizations ranging the ray parameter p from $-0.06s/km$ to $0.06s/km$ with ray parameter step $\triangle p = 0.02s/km$. Fig.16c and d are the imaging results by linear phase encoding method and chirp phase encoding method with 13 realizations ranging the ray parameter p from $-0.06s/km$ to $0.06s/km$ with ray parameter step $\triangle p = 0.01s/km$. 37 sources are arranged from $0.4km$ to $14km$ with a spacing of $0.4km$. Fig.17a and b show the imaging results with 7 simulations by linear phase encoding method and chirp phase encoding method respectively. 71 sources are arranged from

Table1. Image quality evaluation for different phase encoding methods.

Phase Encoding Methods	N_s	Number of Simulations n	Least-squares Error ε
LPEM	37	7	0.2948
	37	13	0.2282
RPEM	37	7	0.5799
	37	13	0.3698
CPEM	37	7	0.3388
	37	13	0.2269

$0.2km$ to $14km$ with a source interval of $0.2km$.

Fig.18a and b show the imaging results for linear phase encoding method $(p = 0)$ and random phase encoding method (one realization) respectively. We can see that the crosstalk noise in the image by random phase encoding method is stronger than that in the image by linear phase encoding method with one simulation. Fig.19a and b show the imaging results by random phase encoding method with 7 and 13 simulations respectively. It is obvious to observe that the subsurface structures in Fig.19b become clearer and the crosstalk noise has been reduced further comparing with Fig.19a.

Fig.20a and b show the imaging results by linear phase encoding method and chirp phase encoding method with 350 sources arranged. We can see that in Fig.20b, the crosstalk noise in the shallow parts of the image is very obvious. Whereas few crosstalk noise can be observed in Fig.20a. If we examine the images in Fig.20a and b further, we can see that the image in Fig.20b has a higher resolution and some parts of the flanks cannot be imaged in Fig.20a, as indicated by the blue arrows.

It is easy for us to observe that with increasing the number of simulations from 7 to 13, the crosstalk noise has been reduced for linear phase encoding method, random phase encoding method and chirp phase encoding method. While it is not obvious for us to tell which phase encoding is better. Hence, we used the least-squares error $\varepsilon = \frac{\|I_{exact} - I_{encoding}\|_2}{\|I_{exact}\|_2}$ to evaluate the quality of the images by different phase encoding methods, where I_{exact} and $I_{encoding}$ indicate the images by traditional shot-profile method and phase encoding methods.

Table.1 shows the least-squares error ϵ comparison for different scaling methods. LPEM, RPEM and CPEM in Table.1 mean linear phase encoding method, random phase encoding method and chirp phase encoding method respectively. We can see that with increasing the number of simulations from 7 to 13, the least-squares errors for the three different phase encoding methods all decrease. And the least-squares errors for random phase encoding method are obviously larger than those by linear phase encoding method and chirp phase encoding method.

CONCLUSION

In this research, the phase encoded anisotropic RTM was implemented and applied on the Hess VTI model. And the imaging results by linear phase encoding method, random phase encoding method and chirp phase encoding method are compared. Several conclusions can be achieved: (a) for fixed ray parameter (e.g.$p = 0$) when the sources are sparsely sampled, with increasing the number of sources, the crosstalk noise becomes more serious, while the amplitudes of the deep reflectors become stronger. And when the sources are densely distributed, few crosstalk artifacts can be observed; (b) for all of the three phase encoding methods, the crosstalk noise can be reduced better, with increasing the number of realizations; (c) with the same number of simulations, the linear phase encoding method and chirp phase encoding method can reduce the crosstalk artifacts better than the random phase encoding method; (d) for dense sources arrangements, the chirp phase encoding method can introduce more crosstalk artifacts than the linear phase encoding method but can achieve image with higher resolution.

ACKNOWLEDGMENTS

This research was supported by the Consortium for Research in Elastic Wave Exploration Seismology (CREWES).

REFERENCES

Baysal, E. D., Kosloff, D. D., and Sherwood, J. W. C., 1983, Reverse time migration: Geophysics, **48**, 1514–1524.

Dai, W., and Schuster, G. T., 2013, Plane-wave least-squares reverse-time migration: Geophysics, **78**, S165–S177.

Du, X., 2007, Prestack depth migration methods for isotropic and polar anisotropic media: Ph.D. thesis, The University of Calgary.

Fletcher, R. P., Du, X., and Fowler, P. J., 1987, The pseudospectral method - comparisons with finite differences for the elastic wave equation: Geophysics, **52**, 483–501.

Fletcher, R. P., Du, X., and Fowler, P. J., 2009, Reverse time migration in titled transversely isotropic (tti) media: Geophysics, **74**, 179–187.

Huang, H., Zhang, Y., and Zhang, H., 2009, The benefit of tti reverse time migration for subsalt imaging, gulf of mexico, 1–5.

Johnston, J. E., and Christensen, N. I., 1995, Seismic anisotropy of shales: Geophysical Prospecting, **46**, 288–297.

Jones, L. E. A., and Wang, H. F., 1987, Ultrasonic velocities in cretaceous shales from the williston basin: Geophysics, **46**, 288–297.

Leslie, J. M., and Kaelin, D. C., 1999, A refraction-seismic field study to determine the anisotropic parameters of shales: Geophysics, **64**, 1247–1252.

Liu, F., Stolt, R. H., Hanson, D. W., and Day, R. S., 2002, Plane wave source decomposition: an accurate [hase encoding scheme for prestack migration, 1156–1159.

Liu, F., Whitemore, D. W., Day, R. S., and Stolt, R. H., 2006, Toward a unified analysis for source plane-wave migration: Geophysics, **71**, S129–S139.

McMechan, G. A., 1983, Migration by exploration of time-dependent boundary values: Geophysical Prospecting, **31**, 413–420.

Morton, S. A., and Ober, C. C., 1998, Faster shot-record depth migrations using phase encodingtest, 1131–1134.

Pan, W., Innanen, K. A., and Margrave, G. F., 2014, Efficient full waveform inversion in the time-ray parameter domain using iteration-dependent sets of ray parameters, 1–4 (submitted).

Romero, L. A., Ghiglia, D. C., Ober, C. C., and Morton, S. A., 2000, Phase encoding of shot records in prestack migration: Geophysics, **65**, 426–436.

Shan, G., 2008, Imaging of steep reflectors in anisotropic media by wavefield extrapolation: Ph.D. thesis, Stanford University.

Shan, G., Clapp, R., and Biondi, B., 2009, 3d plane-wave migration in titled coordinates: A field data example: Geophysics, **74**, WCA199–WCA209.

Tang, Y., 2009, Target-oriented wave-equation least-squares migration/inversion with phase-encoded hessian: Geophysics, **74**, WCA95–WCA107.

Tao, Y., and Sen, M. K., 2013, Frequency-domain full waveform inversion with plane-wave data: Geophysics, **78**, R13–R23.

Thomsen, L., 1986, Weak elastic anisotropy: Geophysics, **46**, 1954–1966.

Tsvankin, I., 1996, P-wave signatures and notation for transversely isotropic media: An overview: Geophysics, **61**, 467–483.

Whitmore, N. D., 1983, Iterative depth migration by backward time propagation, 827–830.

Zhang, Y., Sun, J., Notfors, C., Gray, S. H., Chernis, L., and Young, J., 2005, Delayed-shot 3d depth migration: Geophysics, **70**, E21–E28.